J. Fluid Mech. (2007), *vol.* 593, *pp.* 33–56.
doi:10.1017/S002211200700852X Printed in the United Kingdom

Interaction of lithotripter shockwaves with single inertial cavitation bubbles

EVERT KLASEBOER[1], SIEW WAN FONG[1], CARY K. TURANGAN[1], BOO CHEONG KHOO[2,3]†, ANDREW J. SZERI[4], MICHAEL L. CALVISI[5], GEORGY N. SANKIN[6] AND PEI ZHONG[6]

[1]Institute of High Performance Computing, 1 Science Park Road, #01-01 The Capricorn, Singapore Science Park II, Singapore 117528

[2]Department of Mechanical Engineering, National University of Singapore, 10 Kent Ridge Crescent, Singapore 119260

[3]Singapore-MIT Alliance, 4 Engineering Drive 3, Singapore 117576

[4]Department of Mechanical Engineering, University of California, Berkeley, California 94720, USA

[5]School of Mathematics, The University of Birmingham, Edgbaston, Birmingham B15 2TT, UK

[6]Department of Mechanical Engineering and Materials Science, Duke University, Box 90300 Durham, NC 27708, USA

(Received 13 April 2007 and in revised form 6 August 2007)

The dynamic interaction of a shockwave (modelled as a pressure pulse) with an initially spherically oscillating bubble is investigated. Upon the shockwave impact, the bubble deforms non-spherically and the flow field surrounding the bubble is determined with potential flow theory using the boundary-element method (BEM). The primary advantage of this method is its computational efficiency. The simulation process is repeated until the two opposite sides of the bubble surface collide with each other (i.e. the formation of a jet along the shockwave propagation direction). The collapse time of the bubble, its shape and the velocity of the jet are calculated. Moreover, the impact pressure is estimated based on water-hammer pressure theory. The Kelvin impulse, kinetic energy and bubble displacement (all at the moment of jet impact) are also determined. Overall, the simulated results compare favourably with experimental observations of lithotripter shockwave interaction with single bubbles (using laser-induced bubbles at various oscillation stages). The simulations confirm the experimental observation that the most intense collapse, with the highest jet velocity and impact pressure, occurs for bubbles with intermediate size during the contraction phase when the collapse time of the bubble is approximately equal to the compressive pulse duration of the shock wave. Under this condition, the maximum amount of energy of the incident shockwave is transferred to the collapsing bubble. Further, the effect of the bubble contents (ideal gas with different initial pressures) and the initial conditions of the bubble (initially oscillating *vs.* non-oscillating) on the dynamics of the shockwave–bubble interaction are discussed.

1. Introduction

The formation of a high-speed jet in a collapsing bubble was first suggested by Kornfeld & Suvorov (1944), almost three decades after the initial study of spherically

† Author to whom correspondence should be addressed.

oscillating bubbles by Lord Rayleigh (1917). This jetting phenomenon is caused by a non-uniform fluid flow around the bubble. This flow non-uniformity can be caused by the presence of a boundary near the oscillating bubble. Another mechanism causing jet formation in an oscillating or quiescent bubble (under free-field conditions) is through the interaction of a bubble with an impinging shockwave. For the former, high-speed jets from collapsing bubbles may contribute to the severe damage to ship propellers or pumps (Young 1989; Philipp & Lauterborn 1998), and to structures after underwater explosions (Cole 1948; Klaseboer *et al.* 2005*a*, *b*). In the latter case, the jetting produced by shockwave–bubble interaction is often even more violent and destructive, with a jet velocity up to several $\mathrm{km\,s^{-1}}$ (Bourne & Field 1999; Klaseboer *et al.* 2006*b*). Apart from its destructive nature, cavitation-induced jets can also be harnessed for constructive use, for instance, in a micro-pump system as proposed by Khoo, Klaseboer & Hung (2005) or Lew, Klaseboer & Khoo (2007).

An area where shockwave–bubble interaction has been found to play a critical role is shockwave lithotripsy (SWL), in which high-energy shockwaves are used for non-invasive disintegration of kidney stones in patients (Chaussy, Brendel & Schmiedt 1980; Delius 2000). Among the various mechanisms investigated (Coleman *et al.* 1987; Crum 1988; Delius & Brendel 1988; Gracewski *et al.* 1993; Zhong & Chuong 1993; Zhong *et al.* 1993; Lokhandwalla & Sturtevant 2000; Eisenmenger 2001; Xi & Zhong 2001; Cleveland & Sapozhnikov 2005), cavitation is believed to play an important role in ensuring the successful disintegration of kidney stones to fine fragments for spontaneous discharge (Zhu *et al.* 2002). The interaction of a lithotripter shockwave with either pre-existing bubbles or bubbles produced by preceding lithotripter pulses, may lead to the formation of high-speed jets in the direction of the shockwave propagation, resulting in the generation of a localized stress concentration on the surface of the kidney stones at the bubble collapse site (Xi & Zhong 2000). In addition, cavitation and shockwave–bubble interaction are believed to contribute to renal tissue injuries produced in SWL, although the underlying mechanisms may be substantially different (Philipp *et al.* 1993; Zhong *et al.* 2001; Jamaluddin 2006). Optimization of the shockwave–bubble interaction has been suggested as a means of maximizing stone comminution while minimizing the collateral tissue injury in SWL (Zhong & Zhou 2001; Zhou *et al.* 2004).

Several attempts have been made to understand better the dynamics of shockwave–bubble interaction under well-controlled experimental conditions. For example, Bourne & Field (1992) investigated the collapse of a 6 mm cylindrical air cavity, embedded in a gelatin/water mixture, by a planar shock of 1.88 GPa. Kodama & Takayama (1998) studied the interaction of a spherical shock of about 10 MPa, generated by micro explosives, with a 0.8 mm diameter bubble attached to the surface of a tissue mimicking gel phantom. Jetting was observed in the interaction of shockwaves with micron sized bubbles experimentally by Ohl & Ikink (2003). Although most of the previous studies were concentrated on shockwave interaction with a stationary bubble, Sankin *et al.* (2005) made the first experimental study on shockwave interaction with a laser-generated inertial oscillating cavitation bubble in water. Calvisi *et al.* (2005) reported preliminary results concerning the numerical modelling of these experiments. In particular, Sankin *et al.* (2005) examined the influence of the phase of the bubble oscillation (relative to the impinging shockwave) on resultant jet formation and secondary shockwave generation. They observed a phase-dependent amplification in jet velocity and impact pressure, which could have significant implications not only for SWL, but also for ultrasound-mediated drug and gene delivery (Sankin & Zhong 2006), or other situations involving the interaction of shockwaves with oscillating

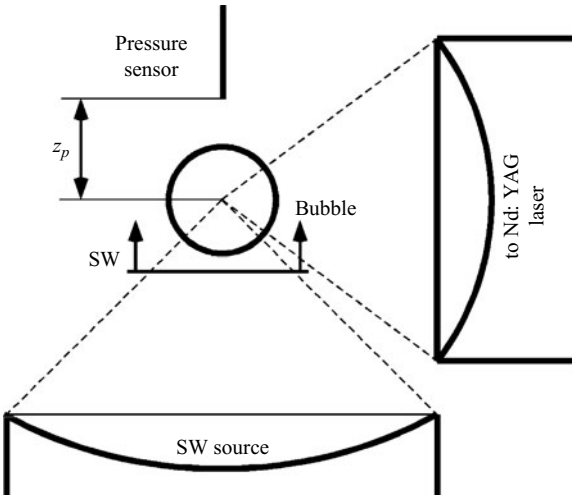

FIGURE 1. Experimental set-up (schematic); a laser-generated bubble in a water tank is being hit by a shockwave (SW) from a piezoelectric shockwave generator. The pressure is measured with a pressure sensor, which is mounted at a distance z_p behind the bubble.

bubbles. In light of these previous studies, it is highly desirable to further develop a numerical model that can be used to simulate shockwave–inertial bubble interaction and the resultant asymmetric collapse and jet formation.

Numerical simulations can capture specific details in the transient shockwave–bubble interaction that are significant and yet difficult or sometimes impossible to obtain experimentally. Several numerical techniques have been used to simulate shockwave–bubble interaction with resultant jet formation, including the free-Lagrange method (Ball *et al.* 2000; Turangan *et al.* 2008), the arbitrary Lagrangian Eulerian method (Ding and Gracewski 1996), and the boundary-element method (BEM) (Calvisi *et al.* 2005; Klaseboer *et al.* 2006*b*). In comparison, BEM is most efficient in terms of the use of storage space and computational time (Klaseboer *et al.* 2006*b*). For the simulation of the interaction of a bubble with a planar shockwave, the computational time for the BEM approach is only several minutes on a common personal computer compared to several days for other methods. The BEM predictions agree favourably with both experimental results and numerical data from the free-Lagrange and arbitrary Lagrangian Eulerian methods. However, the other methods can provide more details about the flow field, such as the reflection of shockwaves, which cannot be obtained using the BEM.

In this work, the BEM model developed by Klaseboer *et al.* (2006*a*, *b*) is extended to simulate the interaction of a shockwave with an initially oscillating cavitation bubble, based primarily on the experimental study of Sankin *et al.* (2005), together with some new experimental results. The paper is organized as follows. In § 2, the experimental set-up is described, followed by the model and the simulation method in § 3. In § 4, the simulation results are compared with experimental observations. The physics and observations from the simulations are discussed in § 5, and finally, the conclusions are given in § 6.

2. Experimental set-up

A schematic diagram of the experimental set-up is shown in figure 1. A Q-switched Nd:YAG laser (wavelength 1064 nm and pulse duration of 3–5 ns) was

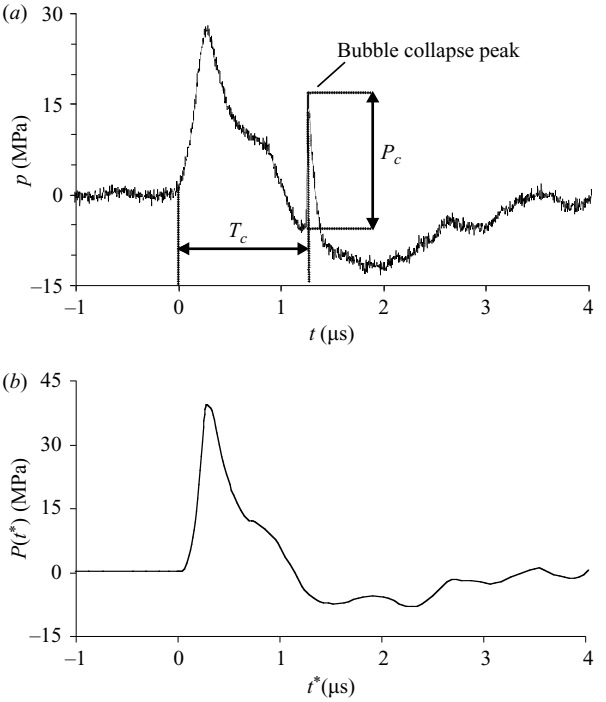

FIGURE 2. (*a*) Typical experimental shockwave profile measured in the fluid in the presence of a bubble, with the bubble collapse peak indicated. The bubble collapse time (T_c) and the bubble collapse pressure peak (P_c) are as indicated. (*b*) Averaged smoothed experimental shockwave profile in the absence of a bubble, $P(t^*)$, as a function of t^* with peak pressure 39 MPa. This profile is used in this paper for the numerical simulations. The pulse has an approximately 1 μs compressive wave followed by a 2 μs tensile wave of −8 MPa. The subsequent secondary oscillations in the profiles are due to reflections.

focused in water to generate a single cavitation bubble ($R_{max} = 300\,\mu$m) via optical breakdown. This method offers excellent control over the maximum bubble radius (there is about 5 % deviation in the maximum radius in the experiments). The laser was aligned horizontally with its beam focus coinciding with the focal point of a piezoelectric shockwave lithotripter (FB12, Richard Wolf). The pressure waveforms were measured using a fibre optic probe hydrophone (FOPH-500, RP Acoustics, Leutenbach, Germany). The 100 μm probe tip of the hydrophone was aligned vertically at a distance $z_p = 1.1$mm from the focus. The hydrophone was thus placed directly behind the bubble, allowing a direct measurement of the secondary shockwave emission produced by the lithotripter pulse–bubble interaction (see e.g. figure 2*a*). The dynamics of the shockwave–bubble interaction were captured using a high-speed imaging system (Imacon 200, DRS Hadland) at a framing rate of 2 million frames per second. Experimental details can be found in Sankin *et al.* (2005).

3. Mathematical model for the shockwave–bubble interaction

This section describes an extension of the mathematical model of shockwave–bubble interaction as introduced by Klaseboer *et al.* (2006*b*). The differences between the current model and that of Klaseboer *et al.* (2006*b*) are the implementation of

a realistic experimental shockwave profile (figure 2*b*) and the use of different initial bubble conditions (oscillating *vs.* non-oscillating bubble).

3.1. *Oscillating bubble prior to its interaction with the shockwave*

Some theoretical results concerning a spherically oscillating bubble, which are used to model the bubble before the shockwave impinges on it, are discussed here. The fluid flow around the bubble will be represented by a velocity potential, Φ, which satisfies the Laplace equation $\nabla^2\Phi = 0$. The gradient of the potential gives the velocity vector $\boldsymbol{u} = \nabla\Phi$. If the bubble is far from boundaries (either free surfaces or solid structures), and in the absence of other disturbances (such as buoyancy for small bubbles), the bubble will oscillate spherically prior to the interaction with the shockwave. Continuity of mass of the fluid around the spherically expanding bubble requires that the radial fluid velocity u_r depends on the radial coordinate d (with its origin in the centre of the bubble) as $d^2u_r = R^2\mathrm{d}R/\mathrm{d}t$, where R and $\mathrm{d}R/\mathrm{d}t$ denote the bubble radius and bubble wall velocity at time t, respectively. Thus, the velocity potential becomes

$$\Phi = -\frac{R^2}{d}\frac{\mathrm{d}R}{\mathrm{d}t}. \tag{1}$$

Assuming that the internal pressure of the bubble, p_b (which originates mainly from its non-condensable gas contents), behaves adiabatically and is uniform across the bubble, then

$$p_b = p_{00}\left(\frac{V_{00}}{V}\right)^{\gamma}, \tag{2}$$

where V is the bubble volume, p_{00} is the internal pressure at initial bubble volume $V_{00}(V_{00} = (4/3)\pi R_{00}^3$, with R_{00} denoting the initial bubble radius) and γ is the ratio of specific heats of the bubble contents. For oscillating underwater explosion bubbles, γ was measured to be 1.25 (Cole 1948). It is assumed here that for laser-generated bubbles, this value will also hold. The vapour pressure, which for slow oscillations can be considered a small constant independent of bubble volume, has been neglected in this analysis, but it can be incorporated in (2) when deemed necessary. More complicated models than (2) for modelling the bubble interior are available in the literature (see for example Szeri *et al.* 2003, in which heat and mass transfer across the bubble surface were taken into account).

Spherically oscillating bubbles have been studied extensively (Rayleigh 1917; Brennen 1995). Usually, the equation of motion of the bubble is described by the Rayleigh–Plesset equation. Applying the unsteady Bernoulli equation at the bubble surface, using (1) and setting the fluid pressure to p_b, leads directly to the simplest form of the Rayleigh–Plesset equation

$$\frac{p_b - p_{ref}}{\rho} = \frac{3}{2}\left(\frac{\mathrm{d}R}{\mathrm{d}t}\right)^2 + R\frac{\mathrm{d}^2R}{\mathrm{d}t^2}, \tag{3}$$

where p_{ref} is the hydrostatic pressure and ρ denotes the density of the surrounding liquid (i.e. water, $\rho = 1000\,\mathrm{kg\,m^{-3}}$). In the current set-up, p_{ref} is equal to the atmospheric pressure (1 bar) such that $p_{ref} = p_{Atm} = 0.1\,\mathrm{MPa}$. Using (2), an analytical solution of (3) exists, which relates $\mathrm{d}R/\mathrm{d}t$ to R as (Brennen 1995)

$$\frac{3}{2}\left(\frac{\mathrm{d}R}{\mathrm{d}t}\right)^2 = \frac{p_{ref}}{\rho}\left(\frac{R_{00}^3}{R^3} - 1\right) - \frac{p_{00}}{\rho\,(\gamma - 1)}\left(\frac{R_{00}^{3\gamma}}{R^{3\gamma}} - \frac{R_{00}^3}{R^3}\right). \tag{4}$$

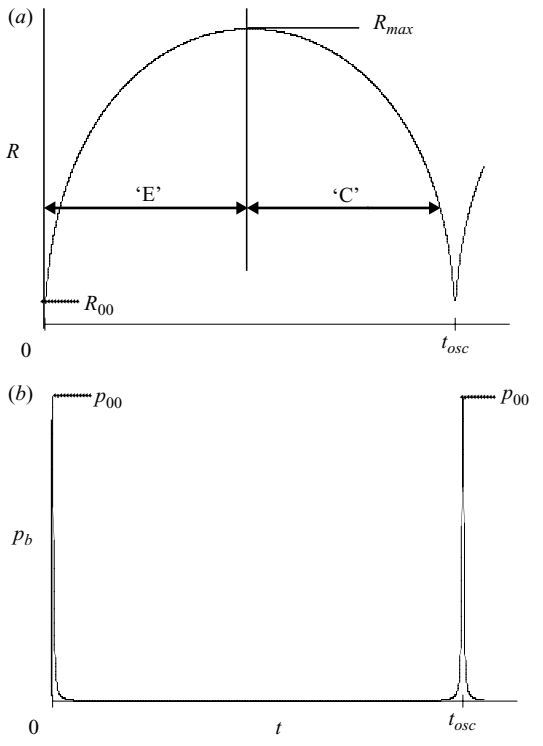

FIGURE 3. (*a*) Typical radius–time (R–t) plot for an oscillating bubble, not interacting with a shockwave, as determined by solving (3) numerically. Following the notation of Sankin *et al.* (2005), we distinguish between an expanding ('E') and collapsing ('C') phase of a bubble. The maximum radius of the bubbles used in this article is $R_{max} = 300\,\mu\text{m}$ and the experimental oscillation time is $t_{osc} = 57.2 \pm 0.8\,\mu\text{s}$ (Sankin *et al.* 2005). (*b*) The pressure inside the bubble, p_b, according to (2). Note the very peaked nature of this pressure; it is $p_b = p_{00}$ for $R = R_{00}$, but almost zero at any other instant.

This equation automatically satisfies the initial condition $\mathrm{d}R/\mathrm{d}t = 0$ at $R = R_{00}$. When the bubble reaches its maximum radius $R = R_{max}$, the velocity becomes again $\mathrm{d}R/\mathrm{d}t = 0$, thus:

$$\frac{R_{00}^3}{R_{max}^3} - 1 = \frac{p_{00}}{p_{ref}} \frac{1}{\gamma - 1} \left(\frac{R_{00}^{3\gamma}}{R_{max}^{3\gamma}} - \frac{R_{00}^3}{R_{max}^3} \right). \tag{5}$$

No analytical solution, however, is known that directly relates R to t. By solving (3) using a Runge–Kutta scheme, a typical bubble radius–time profile can be obtained (figure 3*a*). The bubble starts off with an initial radius R_{00}, grows rapidly to reach a maximum radius R_{max}, then collapses, followed by subsequent rebounds. The bubble's oscillation time, defined as the time from inception through maximum expansion to primary collapse, can be expressed as almost twice the Rayleigh collapse time (Brennen 1995):

$$t_{osc} = 2 \times 0.915 R_{max} \sqrt{\rho / p_{ref}}. \tag{6}$$

The numerical value for t_{osc} is 54.9 μs, based on $R_{max} = 300\,\mu\text{m}$, $\rho = 1000\,\text{kg}\,\text{m}^{-3}$ and $p_{ref} = 0.1\,\text{MPa}$. It corresponds well with the experimental value of 57.2 μs (taking into account the uncertainty range of 5 % of the experimental R_{max}). Using (1), the potential on the surface of an oscillating bubble with radius R_0 (i.e. the radius of

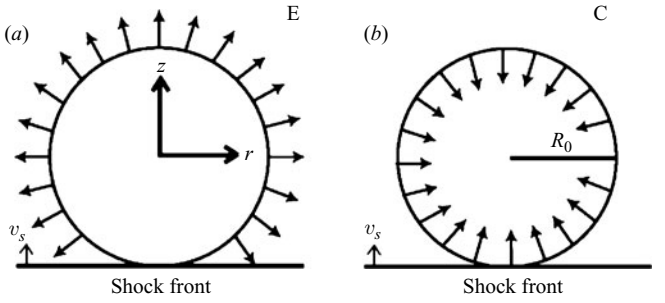

FIGURE 4. Schematic diagram of an upwards moving shockwave hitting a bubble. The shockwave moves upwards with velocity v_s across the bubble. At the moment the shock hits the bubble, the radius of the bubble attains a value R_0. The shockwave hits the lower part of an expanding, or 'E', bubble in (*a*). In (*b*), a collapsing, or 'C', bubble is being hit by the same shockwave.

the bubble at the moment of the shockwave impact) can be determined by setting $d = R = R_0$ and substituting $\mathrm{d}R/\mathrm{d}t$ from (4) as

$$\Phi(R_0) = \pm R_0 \sqrt{\frac{2p_{ref}}{3\rho}\left(\frac{R_{00}^3}{R_0^3} - 1\right) - \frac{2p_{00}}{3\rho(\gamma - 1)}\left(\frac{R_{00}^{3\gamma}}{R_0^{3\gamma}} - \frac{R_{00}^3}{R_0^3}\right)}. \tag{7}$$

The appropriate sign must be chosen in (7): negative for an expanding 'E' bubble and positive for a collapsing 'C' bubble.

A dimensionless parameter ε (often referred to as the strength parameter in bubble dynamics) is defined as

$$\varepsilon = p_{00}/p_{ref}. \tag{8}$$

It is important to note that in (5) only two of the dimensionless parameters ε, R_{00}/R_{max} and γ can be chosen independently. In fact, (5) is used to calculate R_{00} in the numerical model, assuming the other parameters are given. The pressure (p_b) inside an oscillating bubble is shown in figure 3(*b*), which (initially $p_b = p_{00}$) drops below the atmospheric pressure as the bubble expands to its maximum size. Upon collapse, and in the absence of energy dissipation, the pressure will gradually increase, reaching $p_b = p_{00}$ once again as the bubble returns to its original size. The value of p_{00} can easily attain 100 to 500 bar for explosion bubbles (Cole 1948). For convenience, a value $p_{00} = 100$ bar (thus $\varepsilon = 100$) is chosen as the default value in this work, unless otherwise noted. Using (5), we determine the corresponding value of $R_{00}/R_{max} = 0.1485$. It can be shown that the effect of ε on the dynamics of the shockwave–bubble interaction is insignificant (see § 5.2 and the Appendix).

3.2. *Pressure pulse* (*shockwave*)*–bubble interaction*

The simulation of a shockwave as a pressure pulse that interacts with a bubble is depicted schematically in figure 4. The pressure pulse is modelled as a planar wave moving in the z-direction with a constant velocity v_s. Here, v_s is assumed to be the velocity of sound in water, i.e. $v_s = 1500\,\mathrm{m\,s^{-1}}$. The bubble has an initial radius R_0 at the moment of its first interaction with the front of the shockwave, which is moving upwards. The bubble is either in its expansion phase ('E', see also figure 3*a*) or collapse phase ('C') at this instant.

During shockwave–bubble interaction, potential flow is assumed to remain valid, despite the fact that a shockwave is present, and thus the fluid flow around the bubble

will be represented by a velocity potential Φ, as in § 3.1. Owing to potential theory, the unsteady Bernoulli equation applies anywhere in the fluid as well as on the bubble surface (similar to Blake *et al.* 1999):

$$p_b = P(z,t) - \rho \frac{\mathrm{D}\Phi}{\mathrm{D}t} + \tfrac{1}{2}\rho |\boldsymbol{u}|^2, \tag{9}$$

where p_b is defined in (2) and $P(z, t)$ is the far-field reference pressure. The material derivative $\mathrm{D}/\mathrm{D}t = \partial/\partial t + \boldsymbol{u}\cdot\nabla$ is used since the bubble surface is moving with the flow. Buoyancy is ignored owing to the small size (<1 mm) and collapse times (< 4 μs) of the bubbles considered here. Surface tension effects are also neglected since they are usually much smaller than the other pressures in the system (i.e. shockwave peak positive pressure and hydrostatic pressure) in the size range of the bubbles considered in this work. However, for extremely small bubbles (<10 μm), surface tension may become important. In the context of this paper, it is assumed that (2) describes the physics of the gas contents of the bubble correctly, at least in the first approximation for both spherically symmetric and non-spherical bubbles. Some discussion on the validity of the approach of using potential flow and the use of (9) will be given in § 5.3.

For the numerical simulations, a smoothed pressure profile based on experimental measurement, without a laser-generated bubble, was used (figure 2*b*). This shockwave consists of a compressive wave with a peak pressure of 39 MPa for a duration of about 1μs, followed by a tensile wave of −8 MPa for a duration of about 2 μs. This profile is incorporated (similar to the approach followed by Klaseboer *et al.* 2006*b*) both temporally and spatially, into the far-field reference pressure term $P(z,t) = P(t^*)$ in (9) via

$$t^* = t - (z + R_0)/v_s, \tag{10}$$

assuming that $(r, z) = (0, 0)$ corresponds to the centre of the bubble at $t = 0$. If $t^* < 0$, the reference pressure $P(z, t)$ is set to be equal to p_{ref}. The absolute time is equal to $t = 0$ when the front of the shockwave hits the bubble. The initial conditions for the potential of the bubble wall at $t = 0$ are taken from the analytical solution (7) derived from the Rayleigh–Plesset equation, which is a function of the bubble radius R_0at the moment of shockwave impact ($R_{00} < R_0 < R_{max}$). This potential $\Phi(R_0)$ is uniform on the bubble surface prior to the shockwave impact as the geometry of the bubble is still spherically symmetric.

3.3. *Boundary-element method* (*BEM*)

When the shockwave impinges on the bubble at $t = 0$, the spherical symmetry of the bubble will be disrupted and the potential is no longer uniform over the bubble surface. The entire flow field must now be solved using the Laplace equation in the fluid domain. An integral solution of the Laplace equation uses the BEM as (see Blake, Taib & Doherty 1986)

$$c(\boldsymbol{x})\Phi(\boldsymbol{x}) + \int_S \Phi(\boldsymbol{y}) \frac{\partial \mathrm{G}(\boldsymbol{y},\boldsymbol{x})}{\partial n} \mathrm{d}S = \int_S \mathrm{G}(\boldsymbol{y},\boldsymbol{x}) \frac{\partial \Phi(\boldsymbol{y})}{\partial n} \mathrm{d}S. \tag{11}$$

In (11), the potential on the bubble surface, Φ, is related to the normal velocity at this surface, i.e. $\partial\Phi/\partial n = \boldsymbol{n}\cdot\nabla\Phi = \boldsymbol{n}\cdot\boldsymbol{u}$, where $\mathrm{G}(\boldsymbol{y},\boldsymbol{x}) = 1/|\boldsymbol{x}-\boldsymbol{y}|$ represents the free space Green's function. The solid angle, $\mathrm{c}(\boldsymbol{x})$, is viewed from the fluid at a location $\boldsymbol{x}$ on the bubble boundary S. The integrations are performed on the bubble surface S where $\boldsymbol{y}$ is the integration vector. The boundary-element formulation uses the fact that if the potential is known everywhere on the surface S, the normal derivative of the

potential can be determined. For the problem under consideration, an axisymmetric boundary-element method is used (Wang *et al.* 1996). However, the principle as described here is not limited to axisymmetric configurations, but can also be applied to fully three-dimensional cases.

The bubble surface is divided into 50 linear elements using 51 nodes. For each node, (11) will provide an equation between the 51 potentials and normal velocities by piecewise integration on each element. Combining all 51 equations, the unknown normal velocities are solved from the resulting matrix equation. The potentials and normal velocities are also assumed to be distributed linearly on an element. From the potential distribution along the bubble surface, the tangential velocity is obtained. Together with the normal velocity, the velocity vector $\boldsymbol{u}$ can now be constructed. The far-field pressure $P(z, t)$ is known from experiment. From the volume of the bubble, its internal pressure, p_b, can be obtained using (2). The potentials on the bubble surface at the next time step for each node can be obtained from a numerical discretization of (9) with respect to time. The above procedure is continued until the impinging jet of the bubble impacts the bubble's opposite surface. The time step is constant and chosen to be 3×10^{-10} s. The numerical code has been extensively tested in the past for underwater explosions (for example Wang *et al.* 1996) and shockwave–bubble interaction (Klaseboer *et al.* 2006*a*, *b*). It has also been compared to a theoretical solution for non-spherically oscillating bubbles (Klaseboer & Khoo 2006).

4. Results

4.1. *Bubble shape and collapse time*

The upper portions of figures 5(*a*) to 5(*e*) show experimental results for bubbles with $R_0/R_{max} \sim 0.50$ and ~ 0.65 (for both expanding 'E' and collapsing 'C' cases), and one bubble with $R_0/R_{max} \sim 1.0$. Only the bubble shapes immediately before the shockwave impact (left-hand image) and near the moment of minimal bubble volume (right-hand image) are shown, whereas the complete sequence can be found in Sankin *et al.* (2005). All bubbles develop a protrusion in the direction of shockwave propagation (upwards in this case), presumably as a result of the jet impact. Bearing in mind the experimental uncertainty with respect to the time interval of 0.5 μs between successive images, the experimental evidence suggests that smaller bubbles collapse faster than larger ones. For the same size (measured by R_0/R_{max}), the collapse time of a bubble in the expansion phase is longer than its counterpart in the contraction phase. In the case $R_0/R_{max} \sim 1.0$, the bubble flattens during collapse (figure 5*c*).

In the lower half of each panel in figure 5, numerical results corresponding to the experimental observations are presented, together with an additional case for a 'C' bubble with $R_0/R_{max} = 0.16$. The times (in μs) at which the numerical images are taken are indicated. At $t = 0$ μs, just before the shockwave impacts on the lower part of the bubble, the geometry of the bubble is spherically symmetric for all cases. This corresponds to the left-hand image of the experimental data matching the outer most curve for the numerical data.

For the 'C' bubble with $R_0/R_{max} = 0.16$, which corresponds to the smallest initial bubble in the numerical simulations, there is clearly a developing jet, which impacts at $t = 0.48$ μs when the two opposite surfaces of the bubble collide (figure 5*f*). As the collapse time is less than 1 μs, the shockwave is still in its compression stage at the moment of jet impact (see figure 2*b*).

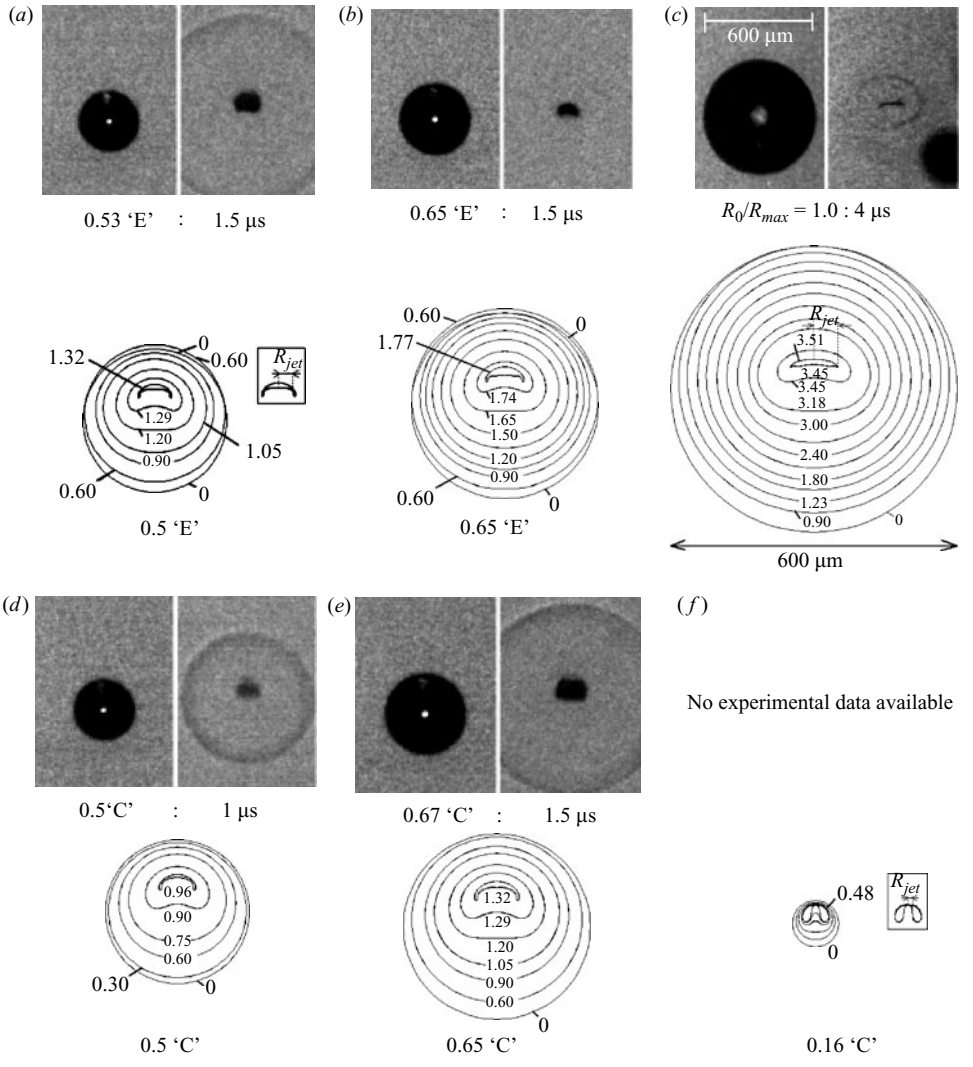

FIGURE 5. Bubble shapes. Experimental: (*a*) $R_0/R_{max} = 0.53$ 'E'; (*b*) 0.65 'E' (*c*) 1.0 (*d*) 0.5 'C'; (*e*) 0.67 'C'. Numerical: (*a*) $R_0/R_{max} = 0.5$ 'E'; (*b*) 0.65 'E'; (*c*) 1.0; (*d*) 0.5 'C'; (*e*) 0.65 'C'; (*f*) 0.16 'C'. The full set of experimental frames can be found in Sankin *et al.* (2005). Numerical and experimental images are not plotted on the same scale. In the experimental results, the image on the left-hand side is taken at $t = 0$ μs (the moment when the shockwave first hits the bubble), while the corresponding image on the right is around the moment of jet impact (time provided below the image). The times corresponding to the numerical images are also indicated in the figures (in μs). The definition of R_{jet} is indicated in figure 5(*a*), (*c*) and (*f*) (the inset with black rectangle).

For bubbles with $R_0/R_{max} = 0.50$ (figure 5*a*, *d*), much flatter and broader jets are developed when compared to the $R_0/R_{max} = 0.16$ case. Although the shapes for an 'E' bubble in figure 5(*a*) and a 'C' bubble in figure 5(*d*) are similar, the collapse times are quite different (0.96 μs for the 'C' bubble and 1.32 μs for the 'E' bubble). Moreover, at the moment of collision, the 'E' bubble has a slightly flatter bottom part, leading to the first contact between the 'top' and 'bottom' surfaces being established further off the axis of symmetry.

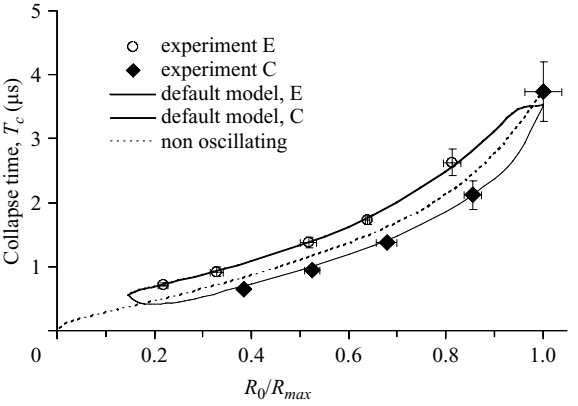

FIGURE 6. Experimental and numerical collapse time T_c (in μs) versus normalized bubble radius (R_0/R_{max}) when lithotripter shockwave–bubble interaction occurs at the expanding 'E' (upper curve) and collapsing 'C' phase (lower curve) of the bubble oscillation. Numerical results are indicated by a continuous line. The dotted line represents the results for an initially non-oscillating bubble non-dimensionalized with $R_{max} = 300\,\mu m$ (see § 5.1).

Similar remarks can be made for the $R_0/R_{max} = 0.65$ cases (figure 5*b*, *e*); the 'C' bubble seems to form a slightly more rounded jet than the 'E' bubble. Again the collapse time is different: in the 'C' bubble, the surface collision occurs at 1.32 μs whereas in the 'E' bubble, it occurs at 1.77 μs. The results of the simulation seem to suggest that the compressive part of the shockwave (~1 μs) has completely passed the bubble prior to the surface collision. Therefore, the tensile pressure component of the shockwave will act on the bubble for a brief moment before the bubble reaches its minimum volume. For the largest initial bubble with $R_0/R_{max} = 1.0$ (figure 5*c*), the jet impacts at 3.51 μs, with a bubble that has a peculiar flat shape, which is also observed in the experiments.

The numerical simulations also indicate, as a result of the shockwave–bubble interaction, an upwards translation of the centroid of the bubble in the direction of the shockwave propagation. This can be observed in figure 5(*b*) for the 'E' bubble with $R_0/R_{max} = 0.65$, when the bubble shapes at $t = 0.00$ μs and $t = 0.60$ μs are compared. During this short duration, the bottom portion of the bubble is contracting while the top portion of the bubble shows an initial expansion before the shockwave reaches the upper pole of the bubble, after which the whole bubble surface contracts. This pressure imbalance of the shockwave–bubble interaction appears to be the main driving force that leads to the upwards translational motion of the bubble. For bubbles with other values of R_0/R_{max}, between 0.16 and 1.00, the general features of the asymmetric collapse are similar to those shown in figure 5 (data not shown).

In figure 6, the experimentally measured collapse times T_c (figure 2*a*) are shown for various values of R_0/R_{max} for both 'E' and 'C' bubbles. For each group of bubbles, the smaller the value of R_0/R_{max}, the faster the bubble collapses. Furthermore, at a given R_0/R_{max}, an initially collapsing bubble consistently collapses faster than an initially expanding bubble. No experimental data is available for very low values of R_0/R_{max} because of the non-spherical distortion of laser-generated bubbles at their early and late stages of oscillation. This deficiency, however, can be overcome by the numerical simulation, which is extended to the minimal value of $R_0/R_{max} = 0.1485$. The numerical 'E' and 'C' curves join at the top right-hand side and at the bottom

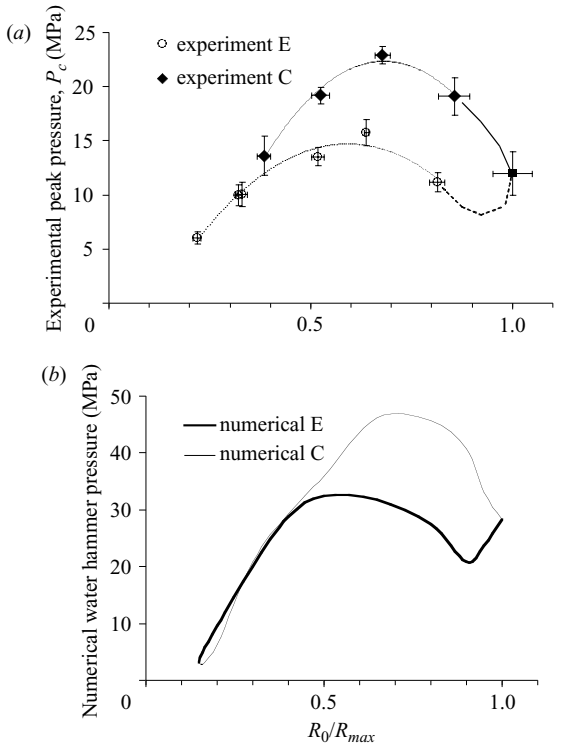

FIGURE 7. (*a*) Experimental peak pressure P_c (see figure 2*a*) versus normalized bubble radius (R_0/R_{max}) when lithotripter shockwave–bubble interaction occurs at the expanding (lower curve 'E') and collapsing (upper curve 'C') phase of the bubble oscillation. The markers indicate actual experimental values and the curves interpolate between these points. (*b*) Numerical water-hammer pressure P_{WH} based on the relative velocity (v_{rel}) and the size of the impacting jet (R_{jet}), both on jet impact, according to (14), simulated with the default model.

left-hand side to form a closed curve. The experimental and numerical results show a close resemblance. Further, the difference in T_c for a pair of 'E' and 'C' bubbles with the same R_0/R_{max} ratio is about 0.5 μs within a large range of R_0/R_{max}.

4.2. *Impact pressure and jet velocity*

The collapse times of the bubbles and the bubble shapes at jet impact are not the only interesting phenomena that can be investigated. The jet velocity and the high-pressure pulse resulting from the impact of these jets are also of practical interest. In figure 7(*a*), the experimentally measured peak pressure shortly after the jet impact is plotted as a function of R_0/R_{max}, which reveals a stronger impact pressure generated by a 'C' bubble than its 'E' bubble counterpart. The highest peak pressures occur at intermediate values of R_0/R_{max}, not in the region of maximum or minimum R_0/R_{max}. The absolute maximum impact pressure occurs for a collapsing bubble around $R_0/R_{max} = 0.7$. As the value of R_0/R_{max} deviates from this optimal number, the impacts pressure drops significantly; for very low R_0/R_{max} values, the peak pressure is only about 1/4 of the maximum value.

Because the numerical model is based on incompressible potential theory, it cannot be used to calculate directly the shockwave emission from the jet impact. However, experimental observations have indicated a direct correlation between jet velocity

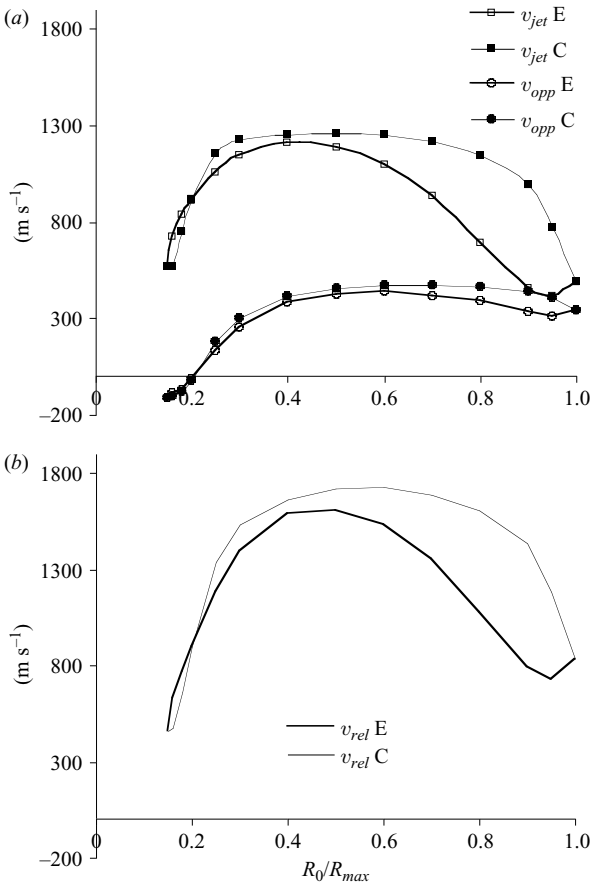

FIGURE 8. (*a*) Numerical jet velocity (v_{jet}) and velocity of the opposite bubble wall (v_{opp}) at the moment of jet impact versus normalized initial radius R_0/R_{max} for expanding ('E') and collapsing ('C') bubbles for the default model with $\varepsilon = 100$. The velocity is taken positive when the bubble wall moves inwards. (*b*) As in figure 8(*a*), but for the numerical relative velocity ($v_{rel} = v_{jet} + v_{opp}$). Experimental data are not available.

and impact pressure (Sankin *et al.* 2005). It is therefore reasonable to compare the numerically calculated maximum jet velocity at the moment of surface collision with the experimentally measured peak pressure. Further, the jet velocity can be used to estimate the water-hammer pressure generated by the surface collision as shown later in this section.

In figure 8(*a*), the numerically calculated jet velocity at the moment of surface collision is plotted as a function of R_0/R_{max} for 'E' and 'C' bubbles. This jet velocity can be extremely high and reaches a maximum value of 1260 m s^{-1} for a 'C' bubble with $R_0/R_{max} = 0.5$. The extreme speeds of the impacting jets are also the reason why they cannot be measured reliably in experiments. Even at the smallest R_0/R_{max} value ($\sim$0.15), the jet velocity is still 570 m s^{-1}. The lowest jet velocity is obtained for $R_0/R_{max} = 0.95$ for an 'E' bubble at 410 m s^{-1}. A careful inspection of figure 8(*a*) reveals that the 'E' and 'C' curves for the jet velocity 'cross over' at $R_0/R_{max} = 0.2$. This means that the jet velocity of an 'E' bubble for $R_0/R_{max} < 0.2$ is larger than a 'C' bubble. For $R_0/R_{max} > 0.2$, the opposite is true. A possible explanation can be found

when figure 6 is investigated more closely: the collapse time differences between 'C' and 'E' bubbles for smaller bubbles are proportionally much shorter than for larger R_0/R_{max}. In other words, for $R_0/R_{max} = 0.2$, the difference is a factor 2, whereas for large R_0/R_{max}, the difference is only 15 to 20 %. A consequence is that the time available to develop high-speed jets for small R_0/R_{max} is comparatively much longer for an 'E' bubble than for a 'C' bubble. Hence, for smaller 'E' bubbles, jets have longer to run, accelerate and achieve higher velocities before impacting onto the opposite bubble wall. The general trend in figure 7(*a*) seems to suggest that such a 'crossing over' at $R_0/R_{max} = 0.2$ may be possible. Overall, a strong resemblance can be seen between figure 7(*a*) and 8(*a*).

Although a jet is developed by the involution of the lower portion of the bubble (see figure 5), the upper portion of the bubble surface (opposite to the side where the jet originates) can also have a non-negligible velocity. For example, the velocity of the opposite bubble wall at the moment of surface collision, v_{opp}, for a 'C' bubble with $R_0/R_{max} = 0.6$ is 475 m s^{-1} (figure 8*a*). The sign for v_{opp} is positive if the upper pole of the bubble moves inwards. For very low values of R_0/R_{max}, v_{opp} can become negative indicating that the upper pole of the bubble is re-expanding once the jet impacts on it. Therefore a relative velocity v_{rel} is defined as:

$$v_{rel} = v_{jet} + v_{opp}. \tag{12}$$

In figure 8(*b*), v_{rel} is plotted as a function of R_0/R_{max}. The general shape of the 'C' and 'E' curves is similar to the jet velocity plots of figure 8(*a*). The relative velocity between the impacting jet and the opposite bubble side is very high and reaches a maximum of around 1730 m s^{-1} for a 'C' bubble with $R_0/R_{max} \sim 0.6$. The relative velocity of figure 8(*b*) also shows a strong resemblance to figure 7(*a*). The maximum values of both the 'E' and 'C' curves occur at the same R_0/R_{max} values for both figures, suggesting that the relative velocity may be a better parameter to correlate with the peak pressure as measured experimentally. The curves for v_{rel} exhibit a minimum near $R_0/R_{max} = 1$, yet the absolute minimum for v_{rel} is obtained at $R_0/R_{max} = 0.15$.

Tomita *et al.* (2002) have used the concept of water-hammer pressure $P_{WH,0}$ (Brunton 1966) to relate v_{rel} with the shockwave pressure produced by the jet impact:

$$P_{WH,0} = \rho v_s v_{rel}/2. \tag{13}$$

If we further assume that $P_{WH,0}$ is confined to an area covered by the impacting jet, and outside this region the impact pressure decays as $1/r$ (which seems to be supported by the images of the expanding shock waves in figures 5*a*, 5*d* and 5*e*), then the peak pressure measured at the location of the hydrophone probe tip ($r = z_p$) would be given by:

$$P_{WH} = \frac{R_{jet}}{2z_p}\rho v_s v_{rel}, \tag{14}$$

where the radius of the jet at the moment of surface collision, R_{jet}, can be obtained from figure 5 and similar plots for other values of R_0/R_{max}. For example, in figures 5(*a*), 5(*c*) and 5(*f*), the definition of R_{jet} is indicated (in the inset with the black rectangle). It is found that R_{jet} increases approximately linearly from 10 μm for $R_0/R_{max} = 0.15$ to 50 μm for $R_0/R_{max} = 1.0$ without much difference between 'E' and 'C' bubbles. For $R_0/R_{max} = 0.53$ (figure 5*a*), the jet radius is about 30 μm, or roughly 3/4 of the horizontal bubble radius at the moment of surface collision. For $R_0/R_{max} = 1.0$ (figure 5*c*), $R_{jet} = 50$ μm and the jet virtually covers the whole width of the bubble. In contrast, for $R_0/R_{max} = 0.16$ (figure 5*f*), the jet is much more slender with $R_{jet} = 10$ μm,

which is about half of the bubble radius at this moment. With the values of v_{rel} and R_{jet}, the variation of P_{WH} for different values of R_0/R_{max} can be calculated as plotted in figure 7(*b*), which reveals a remarkable resemblance to figure 7(*a*). The absolute value of P_{WH}, however, is about twice the measured pressure for large R_0/R_{max}. For small values of R_0/R_{max}, the correspondence is much better with both the numerical and experimental pressures of the order of 5 MPa. This would indicate a peak pressure of 350 MPa at the jet impact site. The highest estimated numerical pressure at the jet impact site is 1290 MPa, which occurs for a 'C' bubble with $R_0/R_{max} = 0.5$. A possible explanation for the discrepancy between the experimental and numerical results of the impact pressure could be the definition of R_{jet}. A close inspection of figure 5 and similar plots reveals that the jet becomes very flat for larger values of R_0/R_{max}. For example, at $R_0/R_{max} = 1.0$ the bubble becomes almost completely flattened towards the end of the collapse phase with the jet occupying the entire bubble width (figure 5*c*). For such a flattened region, the 'effective' R_{jet} could easily be about half the one estimated, thus explaining the difference. Nevertheless, the trends between the experimentally measured pressure of figure 7(*a*) and the numerically calculated one in figure 7(*b*) are very similar.

At the jet impact and shortly afterwards, (14) is not exactly correct since the shockwave emitted by the impacting jet will exhibit a piston-type shockwave profile instead of a radially expanding one. At longer times after the jet impact (equivalent to large z_p), the shockwave emitted from the collapsing bubble behaves as a spherical shock wave. This can be seen from the expanding shockwaves shown in figure 5, and is also confirmed by the numerical simulations by Turangan *et al.* (2008), who used the free-Lagrange method to simulate the shockwaves emitted from a jet in a collapsing bubble. They observed that the piston-type shockwave rapidly turns into a spherical shock wave.

4.3. *Kelvin impulse, kinetic energy and bubble displacement*

The physics of bubble collapse can be further illuminated through calculation of the Kelvin impulse, the kinetic energy and the bubble displacement, all at the moment of jet impact, as considered in this section. These quantities are difficult or even impossible to measure, thereby motivating their calculation through numerical means.

The Kelvin impulse vector $\boldsymbol{K}$ is defined as the integral of the potential on the bubble surface S multiplied by the normal vector $\boldsymbol{n}$ at this surface (Pearson, Blake & Otto 2004):

$$\boldsymbol{K} = \rho \int_S \Phi \boldsymbol{n} \, \mathrm{d}S. \tag{15}$$

For a spherically oscillating bubble the Kelvin impulse vector will be zero, since the potential Φ is then uniformly distributed along the surface of the bubble and $\int_S \boldsymbol{n} \, \mathrm{d}S = \boldsymbol{0}$. Thus, the Kelvin impulse vector gives an indication of the degree of asymmetry in the bubble collapse. Usually, the Kelvin impulse vector has the same direction as the jet. Since the problem under consideration is axisymmetric, the Kelvin impulse vector will only have a component in the z-direction. From now on we will call this quantity $K(= |\boldsymbol{K}|)$. Regarding the Kelvin impulse K, a higher value usually means a higher jet speed or a broader jet. In figure 9, K is plotted for both 'C' and 'E' bubbles at the moment of jet impact for different values of R_0/R_{max}, again with the default bubble model (actually the dimensionless K or K' is plotted, $K = K' R_{max}^3 \sqrt{p_{ref}\rho}$). The 'C' bubbles give a higher value of K' for all values of R_0/R_{max}, except for a very small region with low R_0/R_{max} where again 'crossing' over is observed as for the jet velocity graphs of figure 8 and the water-hammer pressure

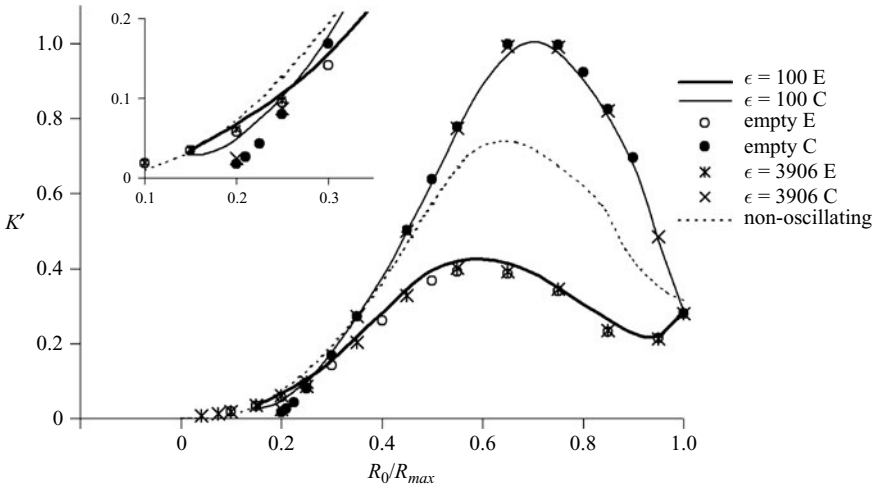

FIGURE 9. The dimensionless Kelvin impulse, K', at the moment of jet impact as a function of R_0/R_{max} for the default bubble with $\varepsilon = 100$ (numerical results). The maximum value of K' appears around $R_0/R_{max} = 0.7$ for a 'C' bubble. The inset shows the typical 'crossing over' for low values of R_0/R_{max}. Also indicated are the results for an empty bubble (§ 5.2), a bubble with $\varepsilon = 3906$ (Appendix) and an initially non-oscillating bubble (dotted line; § 5.1). This figure can be compared to figure 7(*a*).

graph of figure 7(*b*). Both 'C' and 'E' curves show a maximum value for intermediate values of R_0/R_{max} ($R_0/R_{max} = 0.7$ for 'C' bubbles and $R_0/R_{max} = 0.6$ for 'E' bubbles). Very low values of K' are observed for low values of R_0/R_{max}. These trends are similar to those observed for the experimental peak pressure (figure 7*a*) and the relative jet velocity (figure 8*b*); however, the relative jet velocity and K' achieve their maxima at different values of R_0/R_{max}. Thus the Kelvin impulse K' can also be used to predict the qualitative behaviour of the observed experimental pressures.

From the above analysis, it appears that the experimental pressure profiles, as shown in figure 7(*a*), correlate with the relative velocity, the water-hammer pressure and the Kelvin impulse, as similar trends are observed in all these plots. Another useful quantity is the kinetic energy of the liquid, which is defined as

$$E = \frac{\rho}{2}\int_W |\boldsymbol{u}|^2 \,\mathrm{d}W = \frac{\rho}{2}\int_S \Phi \frac{\partial \Phi}{\partial n}\,\mathrm{d}S, \tag{16}$$

where the Gauss theorem is used to convert the integral over the whole fluid domain W into a surface integral over the bubble surface S (see for example Pearson *et al.* 2004 or Klaseboer & Khoo 2006). When the dimensionless kinetic energy E' (made dimensionless with $R_{max}^3 p_{ref}$) at the moment of jet impact is plotted as a function of R_0/R_{max} (figure 10) for the default bubble model, we can see the strong resemblance with figure 9. It appears that if the dimensionless kinetic energy E', is divided by a factor 140, it matches within 5% the dimensionless K' curve. *A priori*, there is no reason why the Kelvin impulse and the kinetic energy should scale; however, they both show similar behaviour at the moment of jet impact. The dimensionless kinetic energy of the bubble at the moment of jet impact reaches a maximum value of about 140. This value is many times higher than the energy of the oscillating bubble system before jet impact, which is roughly $(4/3)\pi R_{max}^3 p_{ref}$ or dimensionless about 4.2 (Klaseboer & Khoo 2006). Thus, around 30 times as much energy as initially

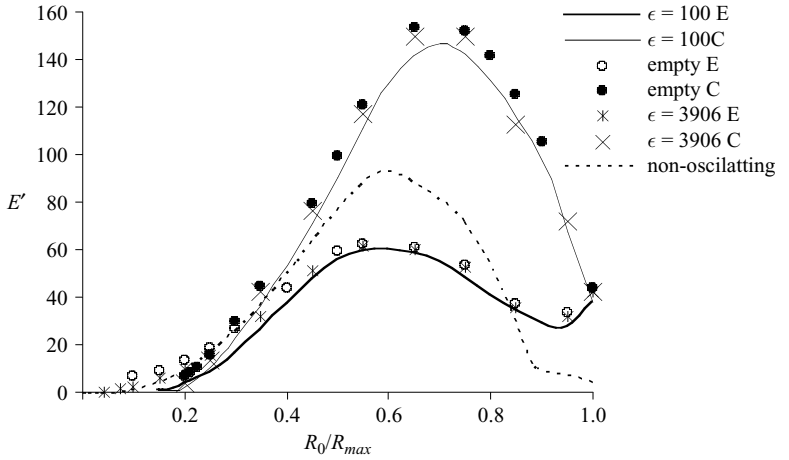

FIGURE 10. The dimensionless kinetic energy at the moment of jet impact, E', as a function of R_0/R_{max} for the default bubble with $\varepsilon = 100$ (numerical results). The maximum value of E' appears around $R_0/R_{max} = 0.7$ for a 'C' bubble. Also indicated are the results for an empty bubble (§ 5.2), a bubble with $\varepsilon = 3906$ (Appendix) and an initially non-oscillating bubble (dotted line; § 5.1). Note the strong resemblance to figure 9.

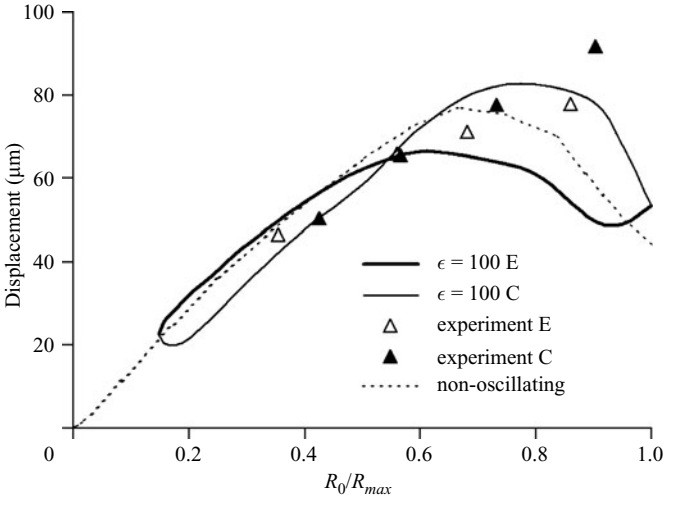

FIGURE 11. The displacement of the bubble centroid at the moment of jet impact as a function of R_0/R_{max} for the experiment (triangles) and the default bubble with $\varepsilon = 100$ (numerical results). The maximum numerical value of the displacement appears around $R_0/R_{max} = 0.8$ for a 'C' bubble. Also indicated are the results for an initially non-oscillating bubble (dotted line; § 5.1).

available has been transferred to the oscillating bubble owing to the interaction with the shockwave.

Not only is a jet generated in the direction of the shockwave, the bubble as a whole is also displaced in this direction. An easily obtainable variable, at least from a numerical point of view, is the displacement of the bubble centroid at the moment of jet impact (figure 11). The largest displacement is observed for a 'C' bubble at $R_0/R_{max} = 0.8$ and reaches a value of about 82 μm. The highest value for an 'E' bubble

is observed for $R_0/R_{max} = 0.65$ at 66 μm. The value $R_0/R_{max} = 0.55$ is a turning point, since the trends are inverted for smaller R_0/R_{max} values where expanding bubbles have a larger displacement at jet impact than collapsing bubbles. An explanation for this phenomenon is that the expanding bubble has a longer period for displacement than a collapsing bubble, as can be seen in figure 6. The 'E' and 'C' curves for the default model join at the left- and right-hand side to form a closed loop in figure 11.

The experimentally obtained values for the displacement are also indicated in figure 11 (these experimental data were not reported in Sankin *et al.* 2005). The experimental displacement is measured as the distance between the centre of the laser plasma and the hypocentre of the shockwave emitted by the collapsing bubble. The order of magnitude of the observed displacements is the same as calculated with the numerical model. Both give displacements of up to about 80 μm.

5. Discussion

5.1. *Comparison with (initially) non-oscillating bubbles*

It is instructive to see the differences between the behaviour of initially oscillating and initially quiescent bubbles. Therefore, the simulations are repeated with a bubble with initial condition $\mathrm{d}R/\mathrm{d}t = 0$ or $\Phi(R_0) = 0$, at the moment of shockwave impact, using the same shockwave profile. The value of $\varepsilon = 1.0$ (instead of the default $\varepsilon = 100$) must now be used to ensure that the parts of the bubble that have not yet been hit by the shockwave stay at rest. The results can be plotted against the same dimensionless R_0/R_{max}, with $R_{max} = 300$ μm again in order to be able to compare the results with the previous sections (R_{max} is not the maximum bubble radius in this case). It appears that the collapse time for a specific value of R_0/R_{max} takes on about the average of the 'C' and 'E' bubbles for the default model (figure 6). For example, a bubble with radius $R_0 = 150$ μm ($R_0/R_{max} = 0.5$), will collapse in 1.11 μs, whereas 'C' and 'E' bubbles with the same R_0/R_{max} value have collapse times of 0.95 and 1.32 μs, respectively. For very small values of R_0/R_{max}, the collapse time tends towards zero.

If the dimensionless Kelvin impulse is investigated (figure 9), the non-oscillating curve is again largely located between the 'C' and 'E' curves, similar to figure 6. This is also the case for the dimensionless kinetic energy at the moment of jet impact (figure 10), except for large values of R_0/R_{max}. Finally, the displacement of the bubble centroid at the moment of jet impact for non-oscillating bubbles is again found to be more or less between the 'C' and 'E' curves (figure 11).

For the default gas bubble model with $\varepsilon = 100$ and $\gamma = 1.25$ (with its corresponding value $R_{00}/R_{max} = 0.1485$) we can easily calculate the minimum pressure when the bubble reaches its maximum volume from (2): $p_{b,min} = 0.078$ bar, a value much lower than the reference pressure $p_{ref} = 1.0$ bar. We might expect that when the pressure inside the bubble is equal to $p_b = p_{ref}$ (for $R/R_{max} = 0.51$), the model for an oscillating and a non-oscillating bubble would give the same results. However, this is not the case, since the fluid around the oscillating bubble is in motion when the shockwave impacts the bubble, whereas the fluid in the non-oscillating case is stationary everywhere at $t = 0$.

5.2. *Sensitivity of the results with respect to the bubble contents: empty bubbles*

In the Appendix, it is shown that a high value of ε has little influence on the results. In this section, the opposite case will be investigated for a zero value of ε, or, in other words, an empty bubble with

$$p_b = 0, \tag{17}$$

instead of (2). This corresponds to a completely empty bubble with no gas or vapour contents (or a vapour bubble with vapour pressure very close to zero). The collapse times show again a very similar trend to the default bubble model (results not shown here). Again, as for the $\varepsilon = 3906$ case (see Appendix), differences can only be observed for R_0/R_{max} values smaller than 0.25. Also, the 'E' and 'C' curves do not join at the bottom to form a closed loop. For $R_0/R_{max} = 0.1$, the bubble appears to collapse spherically, without any jet formation. In figures 9 and 10, respectively, the dimensionless Kelvin impulse and kinetic energy at the moment of jet impact for $\varepsilon = 0$ are plotted. The behaviour for $\varepsilon = 100$, $\varepsilon = 3906$ and the 'empty' bubble are similar for both 'E' and 'C' bubbles. The maxima and the minima appear at the same locations and also the numerical values are almost identical. The displacement of the bubble at the moment of jet impact for the empty bubble case (results not shown) appears to coincide to a large degree with the $\varepsilon = 100$ (figure 11) results.

As shown here and in the Appendix (where a bubble with a very large value of $\varepsilon = 3906$ is investigated), the contents of the bubble do not change the final results significantly with respect to the Kelvin impulse, kinetic energy, etc. at the moment of jet impact. This might be explained by examining the pressure plot of figure 3(*b*). During most of the time, the pressure inside the bubble is very low and can be considered as 'almost empty'. As such, the value of the strength parameter ε has little effect on the results.

5.3. *Efficiency, validity and applications of the BEM model*

The main advantage of our approach using the BEM lies in its efficiency. Typically, this technique needs several minutes on a PC for a full simulation (up to jet impact) as compared to traditional methods that require a much longer time. This is mainly because only a mesh on the bubble is required and not in the fluid domain or in the interior of the bubble. It could be argued that the potential flow approximation is not strictly valid to simulate shockwave–bubble interaction as it is well known that a shockwave by itself cannot be modelled using potential theory. However, Klaseboer *et al.* (2006*b*) argued that the underlying physics of shockwave–bubble interaction is still driven primarily by inertial effects of the surrounding fluid (in this case, water) and, therefore, it is possible to model the shockwave as a pressure perturbation in the liquid. Also, the compressibility of the fluid and internal shockwave in the bubble were found to be of weak, secondary importance. In the foregoing work, the BEM model of shockwave–bubble interaction agreed favourably with experimental data and with results from other numerical methods that took into account these factors. Furthermore, the extended version of this model (as presented in this paper) gives results that correspond very well with experimental data from Sankin *et al.* (2005). For example, using the water-hammer theory, a reasonable estimation for the pressure resulting from the jet impact can be obtained.

A careful investigation of the curves for the experimental and water-hammer pressure (figure 7), the jet and relative velocity (figure 8*b*), the Kelvin impulse (figure 9) and the kinetic energy (figure 10), all at the moment of jet impact, shows that a maximum occurs for intermediate values of R_0/R_{max} (around 0.6 for 'C' bubbles and slightly lower for 'E' bubbles). The collapse time for $R_0/R_{max} = 0.6$ is 1.2 μs for a 'C' bubble and 1.6 μs for an 'E' bubble as can be deduced from figure 6. These times are approximately equal to the duration of the compressive portion of the shockwave ($\sim$1 μs, see figure 2*b*). It therefore seems that the observed maximum occurs for cases in which the entire compressive part of the shockwave acts upon the bubble. For lower values of R_0/R_{max}, only a portion of the available energy is transferred to

the bubble, whereas for higher values of R_0/R_{max}, the tensile part of the shockwave mitigates the effect of the compression. Both of these sub-optimal cases result in collapses with reduced intensity (e.g. jet velocity, pressure, etc.) as compared to the case with intermediate values of R_0/R_{max}. This phenomenon might be exploited in future applications using shockwave–bubble interactions, such as drug delivery, tissue removal, etc.

From the oscillation time of a bubble with a given reference pressure (6), we can estimate the collapse time of the bubble (half the oscillation time) as

$$t_{coll} \sim R_0 \sqrt{\rho / P_{Sh}}, \tag{18}$$

where P_{sh} is a typical pressure as felt by the bubble. In (18), P_{sh} is unknown, but we could use the maximum value of the shockwave as a first approximation. If we take $P_{sh} = 39\,\mathrm{MPa}$ and $R_0 = R_{max}$, then the collapse time according to (18) would be $1.50\,\mu\mathrm{s}$. Numerically, we obtain $3.52\,\mu\mathrm{s}$ (figure 6); thus, (18) underestimates this time. This can be easily explained, since (18) assumes that the pressure around the bubble is P_{sh} during the whole collapse, but in reality the 'effective' pressure is much less, as can be seen in figure 2(*b*). In addition, (18) predicts a linear increase of the collapse time with R_0; however, figure 6 clearly shows an upwards-curving trend. This can be attributed to the fact that for higher values of R_0/R_{max}, the tensile part of the shockwave (figure 2*b*) delays the collapse process and contributes to the upward-curving trends in figure 6.

It is not clear why there are observed differences in the jet shapes for 'E' and 'C' bubbles as shown in figure 5. It appears that 'C' bubbles produce slightly more rounded jet tips than 'E' bubbles, which in turn are flatter (compare for example figures 5*a* and 5*d* or 5*b* and 5*e*). For future applications, however, it might be important to know whether the jet is pointed or broad-crested. The current BEM framework can predict the shape of the jet, its speed and other physical parameters for a given initial bubble size, bubble wall velocity and shockwave profile. This improved insight into the physics of the collapse process may help optimize certain treatments, such as kidney stone removal in shockwave lithotripsy.

6. Conclusions

A model based on the boundary-element method was used to simulate the interaction of a shockwave with an oscillating bubble. The results were validated and compared to experimental results. Collapse times of the experiments and the model show very good agreement. Pressure peaks as measured experimentally due to the impacting jet were compared with a simple water-hammer model also showing good qualitative agreement. In addition, numerical values of the relative velocity (i.e. jet velocity relative to the velocity of the opposite wall), the Kelvin impulse, the kinetic energy and the bubble displacement, all at the moment of jet impact, were calculated showing that the most intense collapses occur for intermediate values of R_0/R_{max}. For these cases, the time scales of the collapse and of the compressive portion of the shockwave are similar, resulting in a maximum transfer of available energy to the bubble. For lower and higher values of R_0/R_{max}, the collapses are not as intense (at least for the particular shockwave profile and maximum bubble radius studied in this work).

The good agreement with experimental data suggests that, although the compressibility of water surrounding the bubble and the internal shockwaves in the bubble are neglected in our model, the model is essentially valid because the whole

phenomenon is dominated by inertia. Other effects are probably of second-order importance only.

A further advantage of using the BEM is a significant reduction in computational time (minutes versus days, as performed on a PC) and effort as compared to other methods such as the free-Lagrange method and the arbitrary Lagrangian Eulerian method. This makes the BEM a useful tool for the study of the interaction of shockwaves (or other pressure perturbations) with bubbles.

This paper was partially written while P. Z. was visiting the Institute for Mathematical Sciences, National University of Singapore in 2007. The experimental work in this study was supported by NIH through grants RO1-EB002682, RO1-DK52985 and S10-RR16802 (PZ), and by Richard Wolf GmbH, Germany by providing the FB12 generator.

Appendix. Sensitivity of the results with respect to the bubble contents: influence of the bubble 'strength'

The exact value of the initial pressure p_{00} for laser-generated bubbles such as those of Sankin *et al.* (2005) is unknown. It is therefore interesting to investigate how the value of ε will influence the numerical results. For a spherically oscillating bubble (without any shockwave), the pressure at a distance d ($d > R$) from the centre of the bubble can be expressed with the help of the unsteady Bernoulli equation, (1) and (3) as (Inoue & Kobayashi 1993)

$$p(d,t) = p_{ref} + \frac{R}{d}\left[\frac{\rho}{2}\left(\frac{\mathrm{d}R}{\mathrm{d}t}\right)^2 + p_b - p_{ref}\right] - \frac{\rho}{2}\frac{R^4}{d^4}\left(\frac{\mathrm{d}R}{\mathrm{d}t}\right)^2. \tag{A 1}$$

At the bubble's minimum radius R_{00} (at $t = 0$ or $t = t_{osc}$), $\mathrm{d}R/\mathrm{d}t = 0$ and (A 1) reduces to

$$p(d,0) = p(d,t_{osc}) = p_{ref} + \frac{R}{d}[p_{00} - p_{ref}]. \tag{A 2}$$

The experimental peak pressures just after the creation of the bubble and at its collapse were measured (without any external shockwave interaction) at a distance of $d = 1.1$ mm away from the bubble. Both peaks have a maximum value of about 4.5 MPa. For underwater explosions (Cole 1948), the first peak is always many times higher than the second. This difference can possibly be explained by the different nature of the contents of the bubble. In principle, it is possible to calculate the pressure inside the bubble just after creation, or p_{00}, from these two peaks. By setting $R = R_{00}$ in (A2) and using (5), we derive the values $\varepsilon = 3906$ and $R_{00}/R_{max} = 0.0413$ at the time of bubble inception. With such a high value of ε (compared to the default value of $\varepsilon = 100$), probably the emission of a shockwave in both expansion and collapse phase occurs (which is also measured by the pressure sensor). Therefore, the value of $\varepsilon = 3906$ as found above is a maximum value and the real value of the internal gas pressure at inception will be much lower. As such, in most of the numerical simulations of the previous sections, we have used the default value of $\varepsilon = 100$.

In order to evaluate the effect of ε, a set of simulations was performed with the value of $\varepsilon = 3906$ and its corresponding $R_{00}/R_{max} = 0.0413$, while keeping all the other parameters constant. For the collapse times, the curves for $\varepsilon = 3906$ and $\varepsilon = 100$ almost coincide for most values of R_0/R_{max} (not shown here). Only for very small

values of R_0/R_{max} can a deviation between the two curves be observed. It is found that for collapsing 'C' bubbles with $R_0/R_{max} < 0.2$, no jet appears for the $\varepsilon = 3906$ case. The pressure in the bubble is so large (3906 bar) that the shockwave has little influence on the bubble dynamics and subsequently no jet is formed. In contrast, for expanding 'E' bubbles, a jet is formed for very small values of R_0/R_{max}. The value 3906 bar (390.6 MPa) is still much smaller than the discussed water-hammer pressure of 1290 MPa of § 4.2, owing to the jet impact.

In figure 9, the dimensionless Kelvin impulse at the moment of jet impact (K') as a function of R_0/R_{max} for $\varepsilon = 3906$ is plotted, together with the results for the default model. For the whole range of R_0/R_{max}, the values of K' with $\varepsilon = 3906$ almost coincide with the $\varepsilon = 100$ curves. Similar remarks can be made for figure 10 where the dimensionless kinetic energy E' is presented at the moment of jet impact for $\varepsilon = 3906$; it strongly resembles its counterpart at $\varepsilon = 100$. The equivalent displacement graph (results not shown here) shows a strong resemblance to the results of figure 11 for $\varepsilon = 100$. Thus, it can be concluded that the value of ε does not greatly influence the numerical results concerning the shockwave–bubble interaction.

REFERENCES

Ball, G. J., Howell, B. P., Leighton, T. G. & Schofield, M. J. 2000 Shock-induced collapse of a cylindrical air cavity in water: a free-Lagrange simulation. *Shock Waves* **10**, 265–276.

Blake, J. R., Taib, B. B. & Doherty, G. 1986 Transient cavities near boundaries. Part 1. Rigid boundary. *J. Fluid Mech.* **170**, 479–497.

Blake, J. R., Keen, G. S., Tong, R. P. & Wilson, M. 1999 Acoustic cavitation: the fluid dynamics of non-spherical bubbles. *Phil. Trans. R. Soc. Lond.* A **357**, 251–267.

Bourne, N. K. & Field, J. E. 1992 Shock-induced collapse of single cavities in liquids. *J. Fluid Mech.* **244**, 225–240.

Bourne, N. K. & Field, J. E. 1999 Shock-induced collapse and luminescence by cavities. *Phil. Trans. R. Soc. Lond.* A **357**, 295–311.

Brennen, C. E. 1995 *Cavitation and Bubble Dynamics*. Oxford University Press.

Brunton, J. H. 1966 High speed liquid impact. *Phil. Trans. R. Soc. Lond.* A **260**, 79–85.

Calvisi, M. L., Szeri, A. J., Sankin, G. N., Zhong, P. & Blake, J. R. 2005 Shock interaction with a growing or collapsing bubble. 58*th Annual Meeting of the American Physical Society, Division of Fluid Dynamics, Chicago, Illinois.*

Chaussy, C., Brendel, W. & Schmiedt, E. 1980 Extracorporeally induced destruction of kidney stones by shock waves. *Lancet* **2**, 1265–1268.

Cleveland, R. O. & Sapozhnikov, O. A. 2005 Modeling elastic wave propagation in kidney stones with application to shock wave lithotripsy. *J. Acoust. Soc. Am.* **118**. 2667–2676.

Cole, R. H. 1948 *Underwater Explosions*. Princeton University Press.

Coleman, A. J., Saunders, J. E., Crum, L. A. & Dyson, M. 1987 Acoustic cavitation generated by an extracorporeal shockwave lithotripter. *Ultrasound Med. Biol.* **13**, 69–76.

Crum, L. A. 1988 Cavitation microjets as a contributory mechanism for renal calculi disintegration in ESWL. *J. Urol.* **140**, 1587–1596.

Delius, M. 2000 History of shock wave lithotripsy. *Proc. 15th Intl Symp. on Nonlinear Acoustics at the Turn of the Millennium.* ISNA 15, 524, pp. 23–32.

Delius, M. & Brendel, W. 1988 A mechanism of gallstone destruction by extracorporeal shock waves. *Naturwissenschaften* **75**, 200–201.

Ding, Z. & Gracewski, S. M. 1996 The behaviour of a gas cavity impacted by a weak or strong shock wave. *J. Fluid Mech.* **309**, 183–209.

Eisenmenger, W. 2001 The mechanisms of stone fragmentation in ESWL. *Ultrasound Med. Biol.* **27**, 683–693.

Gracewski, S. M., Dahake, G., Ding, Z., Burns, S. J. & Everbach, E. C. 1993 Internal stress wave measurements in solids subjected to lithotripter pulses. *J. Acoust. Soc. Am.* **94**, 652–661.

Inoue, Y. & Kobayashi, T. 1993 Nonlinear oscillation of a gas-filled spherical cavity in an incompressible fluid. *Fluid Dyn. Res.* **11**, 84–97.

Jamaluddin, A. R. 2006 Free-Lagrange simulations of shock–bubble interaction in ESWL. PhD thesis, School of Engineering Sciences, University of Southampton, UK.

Khoo, B. C., Klaseboer, E. & Hung, K. C. 2005 A collapsing bubble-induced micro-pump using the jetting effect. *Sensors Actuat.* A **118**, 152–161.

Klaseboer, E. & Khoo, B. C. 2006 Modified Rayleigh–Plesset model for a non-spherically symmetric oscillating bubble with applications to boundary integral methods. *Engng Anal. Boundary Elements* **30**, 59–71.

Klaseboer, E., Hung, K. C., Wang, C., Wang, C. W., Khoo, B. C., Boyce, P., Debono, S. & Charlier, H. 2005*a* Experimental and numerical investigation of the dynamics of an underwater explosion bubble near a resilient/rigid structure. *J. Fluid Mech.* **537**, 387–413.

Klaseboer, E., Khoo, B. C. & Hung, K. C. 2005*b* Dynamics of an oscillating bubble near a floating structure. *J. Fluids Struct.* **21**, 395–412.

Klaseboer, E., Fong, S. W., Turangan, C. & Khoo, B. C. 2006*a* Shockwave non-equilibrium bubble interaction: BEM simulations with experimental comparison. *Proc. Sixth Intl Symp. on Cavitation CAV2006, Wageningen, The Netherlands.*

Klaseboer, E., Turangan, C. K., Fong S. W., Liu, T. G., Hung, K. C. & Khoo, B. C. 2006*b* Simulations of pressure pulse–bubble interaction using boundary element method. *Comput. Meth. Appl. Mech. Engng* **195**, 4287–4302.

Kodama, T. & Takayama, K. 1998 Dynamics behavior of bubbles during extracorporeal shock-wave lithotripsy. *Ultrasound Med. Biol.* **24**, 723–738.

Kornfeld, M. & Suvorov, L. 1944 On the destructive action of cavitation. *J. Appl. Phys.* **15**, 495–506.

Lew, K. S. F., Klaseboer, E. & Khoo, B. C. 2007 A collapsing bubble-induced micropump: an experimental study. *Sensors Actuat.* A **133**, 161–172.

Lokhandwalla, M. & Sturtevant, B. 2000 Fracture mechanics model of stone comminution in ESWL and implications for tissue damage. *Phys. Med. Biol.* **45**, 1923–1940.

Ohl, C. D. & Ikink, R. 2003 Shock-wave-induced jetting of micron sized bubbles. *Phys. Rev. Lett.* **90**, 214502.

Pearson, A., Blake, J. R. & Otto, S. R. 2004 Jets in bubbles. *J. Engng Maths* **48**, 391–412.

Philipp, A. & Lauterborn, W. 1998 Cavitation erosion by single laser-produced bubbles. *J. Fluid Mech.* **361**, 75–116.

Philipp, A., Delius, M., Scheffczyk, C., Vogel, A. & Lauterborn, W. 1993 Interaction of lithotripter-generated shock waves with air bubbles. *J Acoust. Soc. Am.* **93**, 2496–2509.

Rayleigh, Lord 1917 On the pressure developed in a liquid during the collapse of a spherical cavity. *Phil. Mag.* **34**, 94–98.

Sankin, G. N. & Zhong, P. 2006 Interaction between shock wave and single inertial bubbles near an elastic boundary. *Phys. Rev.* E **74**, 046304.

Sankin, G. N., Simmons, W. N., Zhu, S. L. & Zhong, P. 2005 Shockwave interaction with laser-generated single bubbles. *Phys. Rev. Lett.* **95**, 034501.

Szeri, A. J., Storey, B. D., Pearson, A. & Blake, J. R. 2003 Heat and mass transfer during the violent collapse of nonspherical bubbles. *Phys. Fluids* **15**, 2576–2586.

Tomita, Y., Robinson, P. B., Tong, R. P. & Blake, J. R. 2002 Growth and collapse of cavitation bubbles near a curved rigid boundary. *J. Fluid Mech.* **466**, 259–283.

Turangan, C. K., Jamaluddin, A. R., Ball, G. J. & Leighton, T. G. 2008 Free-Lagrange simulations of the expansion and jetting collapse of air bubbles in water. *J. Fluid Mech.* (in press).

Wang, Q. X., Yeo, K. S., Khoo, B. C. & Lam, K. Y. 1996 Strong interaction between a buoyancy bubble and a free surface. *Theor. Comput. Fluid Dyn.* **8**, 73–88.

Xi, X. F. & Zhong, P. 2000 Improvement of stone fragmentation during shock wave lithotripsy using a combined EH/PEAA shock wave generator – In vitro experiments. *Ultrasound Med. Biol.* **26**, 457–467.

Xi, X. F. & Zhong, P. 2001 Dynamic photoelastic study of the transient stress field in solids during SWL. *J. Acoust. Soc. Am.* **109**, 1226–1239.

Young, F. R. 1989 *Cavitation.* McGraw-Hill.

Zhong, P. & Chuong, C. J. 1993 Propagation of shock waves in elastic solids caused by cavitation microjet impact. I: Theoretical formulation *J. Acoust. Soc. Am.* **94**, 19–28.

Zhong, P. & Zhou, Y. F. 2001 Suppression of large intraluminal bubble expansion in shock wave lithotripsy without compromising stone comminution: methodology and in vitro experiments. *J. Acoust. Soc. Am.* **110**, 3283–3291.

Zhong, P., Chuong, C. J. & Preminger, G. M. 1993 Propagation of shock waves in elastic solids caused by cavitation microjet impact. II: Application in extracorporeal shock wave lithotripsy. *J. Acoust. Soc. Am.* **94**, 29–36.

Zhong, P., Zhou, Y. F. & Zhu, S. L. 2001 Dynamics of bubble oscillation in constrained media and mechanisms of vessel rupture in SWL. *Ultrasound Med. Biol.* **27**, 119–134.

Zhu, S. L., Cocks, F. H., Preminger, G. M. & Zhong, P. 2002 The role of stress waves and cavitation in stone comminution in shock wave lithotripsy. *Ultrasound Med. Biol.* **28**, 661–671.

Zhou, Y. F., Cocks, F. H., Preminger, G. M. & Zhong, P. 2004 Innovations in shock wave lithotripsy technology: updates in experimental studies. *J. Urology* **172**, 1892–1898.